ACS APPLIED MATERIALS & INTERFACES

www.acsami.org

Research Article

Gold–Silver Nanoshell-Embedded Polydimethylsiloxane Films for Near-Infrared Photothermal Eradication of Bacteria

Mina Omidiyan, Mengfan Wang, Pooria Tajalli, Xing He, Supawitch Hoijang, Chengzhi Cai, Naihao Chiang,* and T. Randall Lee*

Cite This: *ACS Appl. Mater. Interfaces* 2025, 17, 64065–64076

Read Online

ACCESS | Metrics & More | Article Recommendations | Supporting Information

ABSTRACT: Catheter-related infections (CRIs) pose a significant threat to patient safety; therefore, the development of effective strategies to prevent and treat these infections is imperative. In this study, a photothermal system based on gold–silver nanoshell (AuAgNSh)-modified catheter surfaces was developed for the rapid eradication of the pathogenic bacterium *Enterococcus faecalis* (*E. faecalis*) using near-infrared (NIR) irradiation. The morphology and elemental composition of AuAgNShs were characterized by scanning electron microscopy (SEM), transmission electron microscopy (TEM), energy-dispersive X-ray spectroscopy (EDX), and X-ray photoelectron spectroscopy (XPS). The optical and photothermal properties were acquired by ultraviolet–visible–near-infrared (UV–vis–NIR) spectroscopy and thermographic imaging with an IR camera, respectively. Bacterial survival studies on AuAgNSh-modified surfaces irradiated with and without NIR light were evaluated using a colony-formation assay. The results demonstrated that AuAgNSh-modified surfaces, when illuminated with NIR light, effectively killed *E. faecalis* on silicone surfaces in less than 10 min. The system is stable and reusable throughout multiple cycles and has the potential to serve as a rapid, localized adjunct to traditional antibiotic therapy for CRIs. By harnessing the thermal energy produced by AuAgNShs in response to NIR irradiation, this hyperthermia technique can potentially serve as a broad-spectrum antibiotic that kills adhered pathogens rapidly.

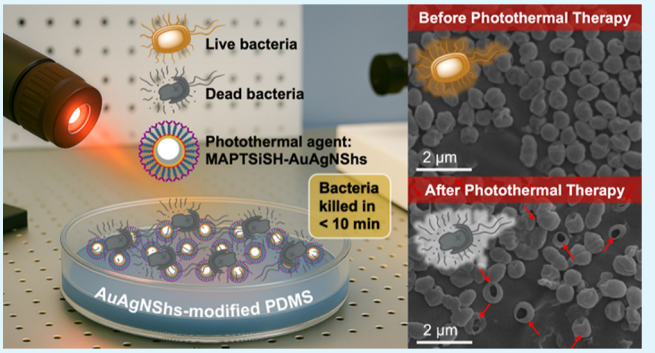

KEYWORDS: *gold–silver nanoshells, photothermal therapy, hyperthermia, bacteria, E. faecalis, laser irradiation, near-infrared (NIR), catheter-related infections (CRIs)*

INTRODUCTION

Nosocomial infections represent a worldwide problem, giving rise to significant financial concerns for hospitals as well as health risks for patients. The National Healthcare Safety Network (NHSN) and Centers for Disease Control and Prevention (CDC) have classified nosocomial infections into 14 distinct categories.[1] Device-associated hospital-acquired infections represent the most common type in clinical settings, with catheter-related infections (CRIs) being a major subset. These infections are linked to microbial adhesion and subsequent biofilm development on catheter surfaces.[1−3] CRIs are associated with an attributable mortality rate of 12−25% and an estimated treatment cost of approximately $56,000 per episode.[4]

Silicone rubber is used to manufacture most indwelling catheters. Bacterial adhesion to silicone surfaces and the consequent generation of biofilms are the primary initiators of disease.[5] As a consequence, strategies have been developed to inhibit pathogenic colonization on silicone catheters and reduce the frequency of CRIs by the use of antibiotics,[6,7] catheter flushes,[6] and antiseptic devices.[8,9] However, as several studies have shown, the formation of the protective matrix increases the resilience of the enclosed bacteria, making them far more resistant to conventional antibacterial and antimicrobial therapies.[10−12] With the rise in antibiotic resistance in nosocomial infections, nanoparticles (NPs), particularly metallic NPs, offer an alternative due to their unique qualities, such as high reactivity and stability.[13,14] To this end, strategies such as silver nanoparticle- and antibiotic-based coatings have been investigated to prevent microbial colonization on catheter surfaces and reduce the incidence of CRIs.[15−18] However, results on their long-term efficacy have been unsatisfactory.[19] In short, it is critical to develop novel approaches for limiting the proliferation of these pathogenic microorganisms on siloxane surfaces.

Received: June 17, 2025
Revised: September 10, 2025
Accepted: October 10, 2025
Published: November 18, 2025

https://doi.org/10.1021/acsami.5c11932
ACS Appl. Mater. Interfaces 2025, 17, 64065−64076

Scheme 1. Proposed Reaction between Silver Nanoparticles and K-Gold Solution and Functionalization of the AuAgNShs with MAPTSiSH

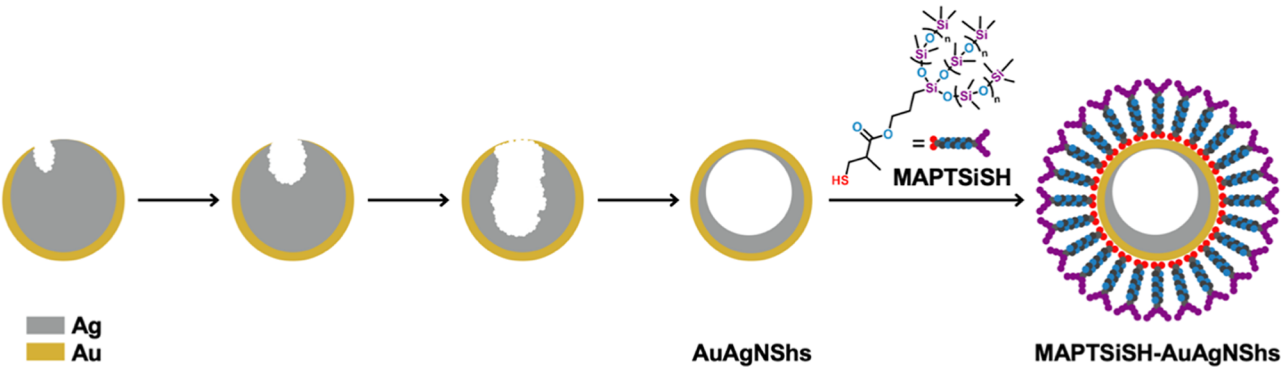

Scheme 2. Photothermal Eradication of Bacteria

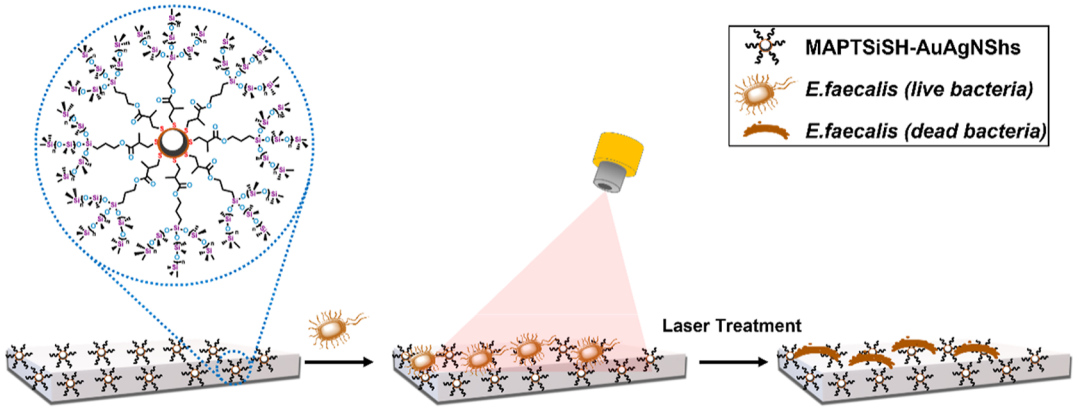

Photothermal therapy (PTT) is a potential technique for physically destroying microorganisms with the minimum toxic effects.[20−23] The crucial feature of this procedure is the employment of photothermal agents that can absorb light and convert it to heat, which is used to destroy harmful bacteria.[23−26] Recently, the use of noble metal NPs as the photothermal agent (PTA) has attracted a lot of attention due to their unique properties, particularly their ultrasmall size (5−200 nm) and remarkable plasmonic properties.[27−29] Among noble metal NPs, the biocompatible and nontoxic gold NPs (AuNPs) are particularly promising candidates for this application due to their capacity to generate hot electrons via the strong localized surface plasmon resonance (LSPR).[28,30] Apart from the significant LSPR effect, another advantage of AuNPs is their tunable light absorption, which can be controlled by the particle's size, shape, composition, and morphology.[30] The photothermal properties of AuNPs have been reported for gold spheres,[31] gold nanoshells (AuNShs),[32−35] gold nanorods,[36,37] and, more recently, gold nanocages[37,38] and gold nanostars.[39−41] Among the various AuNPs, AuNShs have been extensively studied due to their distinctive properties, such as significant surface plasmon absorption and biocompatibility.[42] The optical extinction of traditional nanoshells can be tuned, but is still limited largely to the visible spectrum.

To achieve deeper tissue penetration with minimal absorption by water, the Lee group developed a galvanic replacement method for producing bimetallic Au/Ag shell/core NPs with a partially hollow core structure, extending the optical extinction to significantly longer wavelengths.[43] Unlike metal alloy NPs, the optical absorption of these gold−silver nanoshells (AuAgNShs) can be precisely tuned to desired wavelengths by altering the shell geometry and elemental composition.[27] For the AuAgNSh system, the tuning can most readily be accomplished by increasing the galvanic replacement of Ag by Au, which progressively red-shifts the LSPR into the near-infrared as demonstrated previously.[43] Moreover, the coexistence of two metals with distinct light-absorption characteristics results in extinction spectra spanning a wide visible-to-near-infrared range, making them powerful and effective photothermal agents compared to conventional plasmonic gold nanostructures (e.g., spherical NPs and nanorods).[42,43]

In studies utilizing AuNShs as photothermal agents, the Lee group reported a photothermal system based on carboxylic acid-terminated thiol-functionalized AuNShs covalently attached to amino-functionalized polydimethylsiloxane (PDMS) surfaces as model catheter surfaces and tested their effectiveness at killing the bacterium *Enterococcus faecalis* (*E. faecalis*).[32] This initial system, albeit effective, suffered from the design of having the nanoshells attached to the surface of PDMS, which can potentially allow the detachment and release of the nanoshells into the surrounding medium, thereby degrading the model catheters over time.

In the present study, we demonstrate a new class of PDMS-based materials wherein AuAgNShs are embedded in the model catheter PDMS matrix, leading to a markedly more stable system with photothermal agents uniformly distributed throughout the PDMS. However, embedding metal NPs in a polymer matrix presents significant challenges, including the

https://doi.org/10.1021/acsami.5c11932
ACS Appl. Mater. Interfaces 2025, 17, 64065−64076

possible diffusion and loss of such NPs from the polymer matrix.[44] Therefore, we coated the AuAgNShs with a unique PDMS-compatibilizing agent, thiol methacryloxypropyl T-structure siloxane (MAPTSiSH), for stabilization within PDMS. Scheme 1 shows the galvanic substitution interaction between Ag(0) NP cores and a Au(III) K-gold solution and the structure of MAPTSiSH, which we designed as adsorbates for generating PDMS-compatible self-assembled monolayers (SAMs). In recent work,[45] we demonstrated that SAMs generated from MAPTSiSH on flat gold surfaces can serve as interfacial PDMS mimics and compatibilizing agents.

In our experimental approach, spherical AgNP templates were synthesized through the reduction of silver salts with the mild reducing agent sodium citrate. These spherical NPs were then utilized as templates to grow ultrasmall hollow AuAgNShs at room temperature using a potassium-containing basic solution of gold salt, referred to as K-gold solution.[43] The AuAgNShs were functionalized with the PDMS-compatibilizing adsorbate (MAPTSiSH), and the MAPTSiSH-functionalized nanoshells were blended at varying concentrations into the PDMS matrix to afford a smart antibacterial surface with NIR-activated photothermal bacteria-killing capability. Subsequently, a strain of drug-resistant *E. faecalis*, a commonly found uropathogen,[46] was utilized to demonstrate the efficiency of employing AuAgNSh-modified PDMS surfaces for killing pathogenic bacteria by exposure to NIR light. Scheme 2 shows the overall strategy developed in this study.

The morphology and elemental composition of AuAgNShs were examined by using transmission electron microscopy (TEM), scanning electron microscopy (SEM), energy-dispersive X-ray spectroscopy (EDX), and X-ray photoelectron spectroscopy (XPS). UV−visible−near-infrared (UV−vis−NIR) spectroscopy was used to measure the optical properties of AuAgNShs, MAPTSiSH-AuAgNShs, and AuAgNSh-modified PDMS surfaces. The photothermal properties of the AuAgNSh-modified surfaces were evaluated with an IR thermal imaging camera. On PDMS and AuAgNSh-modified PDMS surfaces, colony formation assays were performed with and without NIR irradiation to determine the bacterial viability. Our findings indicate that silicone surfaces with embedded MAPTSiSH-functionalized AuAgNShs offer considerable promise as an effective approach for in situ elimination of catheter-related nosocomial infections.

EXPERIMENTAL SECTION

Materials. Polydimethylsiloxane base and curing agent (SYLGARD 184 Silicone Elastomer Kit, Dow Corning), silver nitrate, ($AgNO_3$, Sigma-Aldrich), trisodium citrate (EM Science), hydrogen tetrachloroaurate(III) hydrate ($HAuCl_4 \cdot H_2O$, Strem), potassium carbonate (K_2CO_3, J. T. Baker), nitric acid (EM Science), hydrochloric acid (EM Science), Luria−Bertani (LB) medium (BD Difco), phosphate-buffered saline (PBS, Sigma-Aldrich), sodium dodecyl sulfate (SDS, J. T. Baker), and ascorbic acid (Sigma-Aldrich) were purchased from the indicated suppliers and used without purification. Water was purified to a resistivity of 18 MΩ·cm, Millipore water; Academic Milli-Q Water System, Millipore Corporation. Prior to use, every piece of glassware used in the synthesis was cleaned with aqua regia solution ($HCl:HNO_3$; 3:1), rinsed with Milli-Q water, and dried.

Preparation of Silver Nanoparticle Cores. To produce AgNPs, the potassium iodide (KI)-assisted ascorbic acid/citrate reduction protocol[43] and the Lee and Meisel method[47] were used. Initially, 1 mL of a 5 mM aqueous solution of ascorbic acid was added into boiling water, and the mixture was boiled for an additional minute. In a separate solution, $AgNO_3$ (0.0167 g, 0.100 mmol) was dissolved in water, followed by the addition of 2 mL of 1% trisodium citrate solution and 50 μL of 7 μM KI solution. The mixture was sonicated for 5 min and then injected into a boiling ascorbic acid solution. The solution was stirred and refluxed for 1 h at 120 °C. The color of the solution quickly changed from colorless to yellow and turned yellowish-green after 5 min, indicating the presence of AgNPs. After cooling to room temperature, the solution was centrifuged at 8000 rpm for 15 min, and the NPs were dispersed again in 12.5 mL of water.

Preparation of Hollow Gold−Silver Nanoshells. The method used for synthesizing hollow AuAgNShs was adapted from a previously reported procedure.[48] The process involved using a gold salt (K−Au) solution as the reducing agent. First, K_2CO_3 (0.025 g) was added to 100 mL of water, followed by an injection of 2 mL of 1% $HAuCl_4 \cdot H_2O$ solution after 5 min of vigorous stirring. The mixture changed color from yellow to colorless after 30 min of reaction, and the flask was covered with aluminum foil and refrigerated overnight before use. To create hollow AuAgNShs, 100 mL of K−Au solution was added to 10 mL of AgNP solution under vigorous stirring, which led to the deposition of Au on the AgNPs and etching of their cores. After 5 h, the solution was centrifuged at 8000 rpm for 15 min, and the resulting nanoshells were redispersed in 10 mL of water at a concentration of $1.0 \times 1 \times 10^{10}$ particles per mL.

Functionalization of Gold−Silver Nanoshells with MAPTSiSH. To functionalize AuAgNShs with MAPTSiSH, 1.5 mL of MAPTSiSH (1 mM in tetrahydrofuran) was added to 15 mL of a colloidal suspension of AuAgNShs, and the mixture was stirred overnight. The particles were then separated from the solution via centrifugation at 8000 rpm for 10 min.

Solvent Stability Study. We tested ten solvents, including ethanol (EtOH), methanol (MeOH), dimethylformamide (DMF), water (H_2O), hexane, diethyl ether, chloroform ($CHCl_3$), o-xylene, isopropyl amine (IPA), and triethylamine (TEA), in an effort to identify which solvent was the most effective at dispersing AuAgNShs while remaining stable and compatible with PDMS. Our studies found that EtOH was the optimal choice for stability of the AuAgNShs and compatibility with PDMS.

Preparation of PDMS Films. Following the manufacturer's directions, blank PDMS samples were synthesized by combining the elastomer and cross-linker in 10:1 ratio. In order to synthesize PDMS with embedded AuAgNShs, five different amounts of colloidal suspension of functionalized AuAgNShs in EtOH were added to the elastomer/cross-linker combination. The mixture was stirred until the colloid was uniformly distributed, and then it was transferred to a blot box container with a diameter of 3 × 3 cm and cured overnight at 50 °C. The elastomer/cross-linker quantities used were calculated to obtain final samples 3 cm in diameter and 2 mm thick. Sedimentation was minimized by using only 300 μL of the EtOH-dispersed MAPTSiSH-AuAgNShs blended with 3.0 g of viscous PDMS prepolymer (10:1 base/cross-linker) and hand-mixed for approximately 2 min until visually uniform. The slurry was then cast into a 3 cm × 3 cm mold that yielded a film just 2 mm thick, which was placed immediately in a 50 °C oven. Gelation began within minutes, and the rapidly rising viscosity "locked" the nanoshells in place long before gravity could induce noticeable settling.

Prior to biological testing, all PDMS and AuAgNSh-PDMS films were sterilized by immersion in 70% ethanol for 20 min, rinsed twice with sterile PBS, air-dried in a laminar-flow hood, and then transferred aseptically to sterile 24-well plates; control incubations confirmed the sterility of blank films (no growth after 72 h in LB).

Preparation of Bacterial Strain. A single colony of pathogenic *E. faecalis*, isolated from a human bloodstream infection, was grown in 25 mL of LB medium supplemented with tetracycline (4 μg mL^{-1}). Following overnight incubation at 37 °C, the bacterial culture was adjusted to an optical density of 0.25 at 600 nm (OD600), which corresponded to a bacterial concentration of 10^8 CFU mL^{-1}.

Adherence Assay of *E. faecalis*. To evaluate the adhesive capability of *E. faecalis* to AuAgNSh-modified PDMS surfaces, a visual assessment was conducted by using an optical microscope. Each surface was placed in a separate well in a 24-well plate that contained

https://doi.org/10.1021/acsami.5c11932
ACS Appl. Mater. Interfaces 2025, 17, 64065−64076

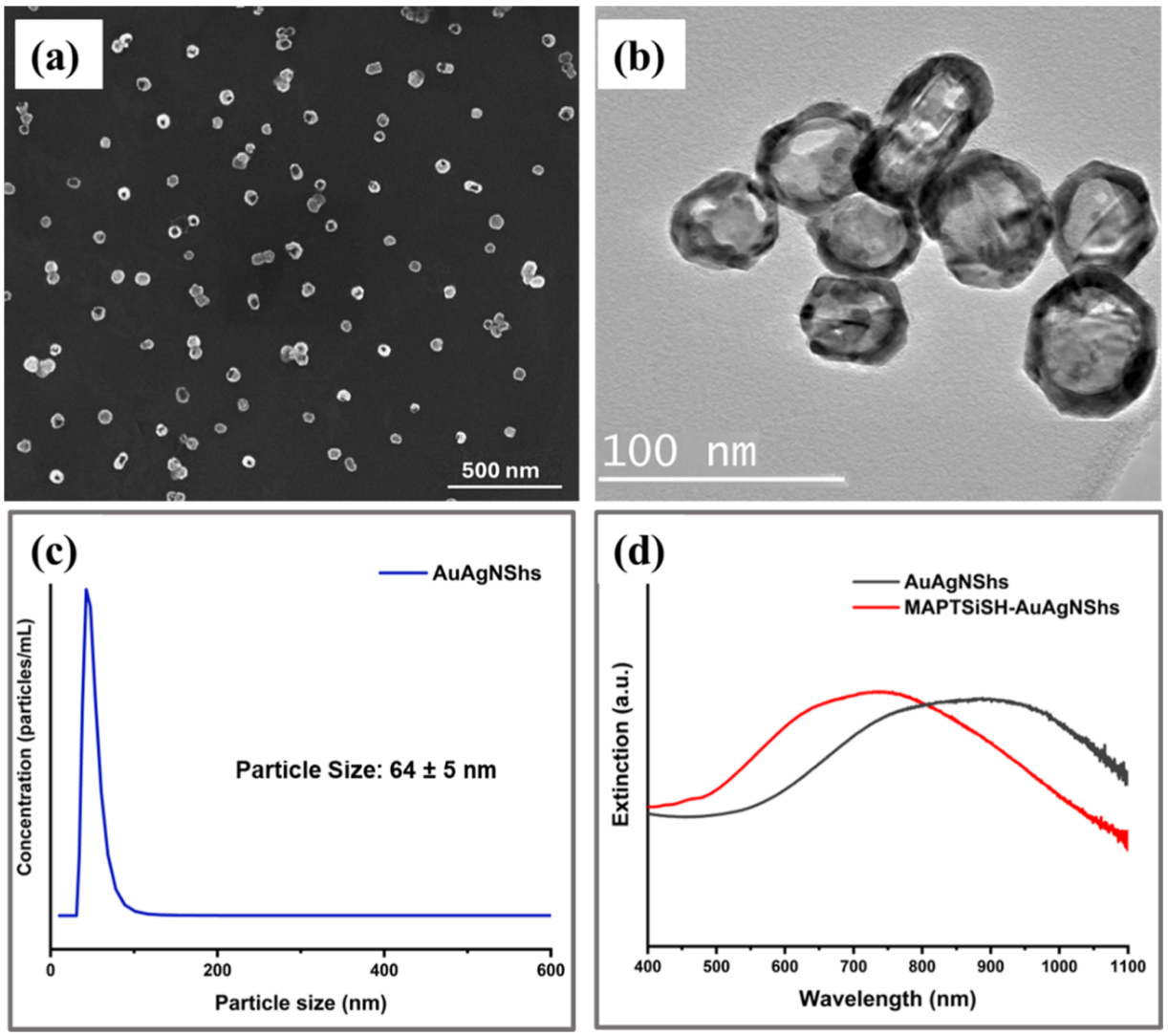

Figure 1. (a) SEM image, (b) TEM image, (c) hydrodynamic diameter distribution of AuAgNShs, and (d) extinction spectra of AuAgNShs (black) and MAPTSiSH-AuAgNShs (red) in water.

1 mL of *E. faecalis* in LB media, with a concentration of 10^8 CFU mL^{-1}. The bacterial cultures were incubated with the surfaces for 72 h at 37 °C. After incubation, the surfaces were washed three times with PBS and then imaged using a 40× objective lens on a Nikon Eclipse Ts2-FL Inverted Microscope.

Photothermal Analysis of AuAgNSh-Modified PDMS Surfaces Targeting *E. faecalis*. To assess the photothermal characteristics of PDMS surfaces modified with AuAgNShs, the films were cut into small sizes of 0.2 × 1 cm and tested for their ability to eliminate *E. faecalis* bacteria. The surfaces were placed in separate wells of a 24-well plate containing LB media with *E. faecalis* at a concentration of 10^8 CFU mL^{-1} and then incubated for 72 h at 37 °C. After incubation, the surfaces were rinsed with PBS and irradiated with a laser (AixiZ HLM5768120; 810 ± 10 nm; 800 mW, continuous wave) at a power density of 2.5 W cm^{-2} for various durations (0, 10, 30, 60, 240, 420, and 600 s). On exposed surfaces, standard plate-based counting was used to determine the number of viable bacteria remaining after treatment. Specifically, the surfaces were sonicated for 10 min in a 0.01% SDS solution using a Bransonic ultrasonic cleaner (50 Hz, 80 W), followed by vortexing for 1 min at 2000 rpm. The resulting bacterial suspension was serially diluted (10^{-2}, 10^{-4}, and 10^{-6}), and 150 μL of each dilution was spread in duplicate on LB agar plates containing 4 μg mL^{-1} tetracycline. The plates were incubated at 37 °C for 24 h, after which bacterial colonies were enumerated.

Bacterial Morphology Assessment Using SEM. Imaging by SEM was used to monitor the bacterial morphology on AuAgNSh-modified PDMS surfaces before and after NIR light exposure. Similar to a previous study,[32] the surfaces were first fixed with 2.5% glutaraldehyde for 18 h, and then washed with PBS. Afterward, the surfaces were postfixed with 1% OsO_4 for 2 h, washed again with PBS, and dehydrated in ascending ethanol concentrations (50%, 70%, 85%, 95%, and 100%) for 10 min each. The samples were then placed in 100% *t*-butanol for 20 min, freeze-dried using a ScanVac CoolSafe 110−4 (LaboGene), sputter-coated with gold (Denton Desk II Desktop Sputtering System), and subsequently analyzed using SEM.

Infrared Thermal Imaging. A PDMS surface modified with AuAgNShs was irradiated by using a diode laser (AixiZ HLM5768120; 810 ± 10 nm; 800 mW, continuous wave). Thermal maps were recorded from at least four distinct surface regions. IR thermal images were acquired with a thermographic camera (ThermoVision A320G, FLIR Systems).

Characterization Methods. The size and morphology of AuAgNShs were characterized by using SEM (LEO 1525, 15 kV accelerating voltage) and TEM (JEOL 2000 FX, 200 kV accelerating voltage). For SEM imaging, samples were deposited onto silicon wafers and air-dried prior to analysis. For TEM, AuAgNShs were drop-cast onto 300-mesh holey carbon-coated copper grids and dried.

Dynamic light scattering (DLS) measurements were performed by using an ALV-5000 Multiple Tau Digital Correlation instrument

https://doi.org/10.1021/acsami.5c11932
ACS Appl. Mater. Interfaces 2025, 17, 64065−64076

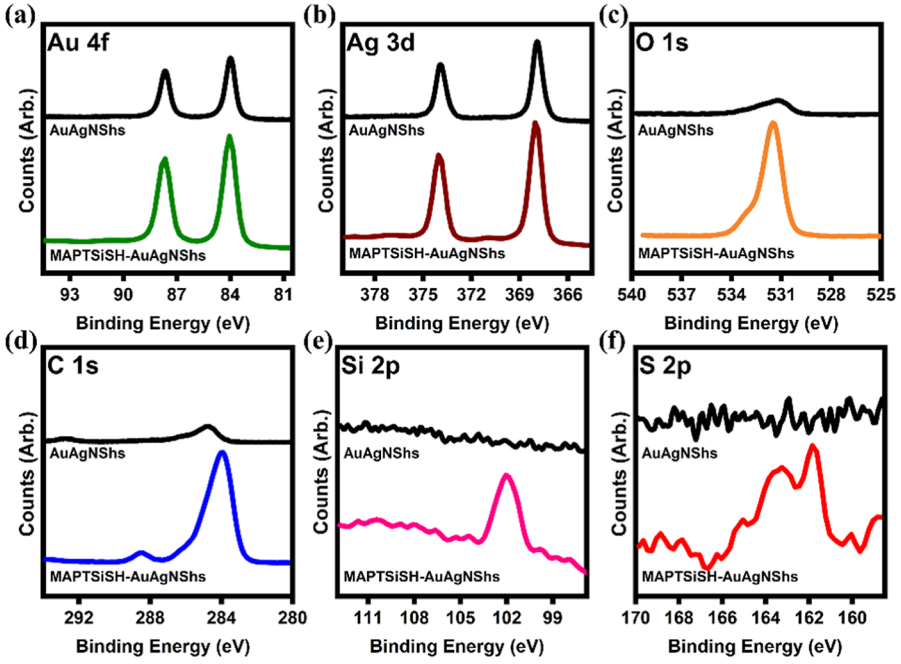

Figure 2. XPS spectra of AuAgNShs (black lines) and MAPTSiSH-functionalized AuAgNShs (colored lines) in the binding energy regions of (a) Au 4f, (b) Ag 3d, (c) O 1s, (d) C 1s, (e) Si 2p, and (f) S 2p.

equipped with a 514.5 nm laser source and a fixed 90° scattering angle. The measured hydrodynamic diameters were consistent with values obtained from SEM and TEM. Nanoparticle tracking analysis (NTA) was carried out using a NanoSight NS300 (NanoSight, Malvern) with laser excitation at 405, 488, 532, and 640 nm. Samples were introduced into the sample chamber by using a sterile syringe (NORM-JECT Tuberculin), and data were collected and processed with NTA 3.1 software under ambient conditions.

The chemical composition of AuAgNShs was determined using EDX (Oxford EDX coupled to LEO SEM). Zeta potential measurements were performed with a Malvern zetasizer to assess the surface charge of the AuAgNShs and MAPTSiSH-AuAgNShs. The surface chemistry of functionalized NPs was examined by XPS (PHI 5700, PHI Instruments) using a monochromatic Al Kα X-ray source. Optical properties were evaluated with a Cary 50 UV−vis−NIR spectrophotometer over a spectral range of 200−1000 nm for both functionalized and nonfunctionalized AuAgNShs.

RESULTS AND DISCUSSION

Preparation and Characterization of AuAgNShs. The synthesis of AuAgNShs was carried out in two steps. Initially, AgNPs were formed from a silver nitrate solution with sizes ranging between 40 and 50 nm; see Figure S1. To avoid the formation of silver nanorods, the addition of potassium iodide and ascorbic acid to the reaction mixture is crucial, while also maintaining strict control over the concentration and temperature. The procedure yielded homogeneous spherical silver particles with high reproducibility, being successful in at least eight out of ten trials, with negligible formation of nanorods. After the AgNPs were obtained, we employed a galvanic replacement technique with a K−Au solution to produce hollow AuAgNShs. During this procedure, gold was deposited on the surface of the AgNPs, leading to the formation of porous AuAgNShs by etching their interiors. The SEM and TEM images (Figure 1a,b) indicate the production of hollow spherical nanoshells. As measured by DLS (Figure 1c), the average hydrodynamic diameter of the AuAgNShs was 64 ± 5 nm, with a polydispersity index (PDI) of 0.20. The plasmon resonance of the hollow AuAgNShs could be tuned to desired visible and NIR wavelengths. As shown in Figure 1d, the extinction spectrum of the AuAgNShs was recorded using UV−vis−NIR spectroscopy over the range of 400−1100 nm. Our AuAgNShs displayed a broad absorption band between 700 and 1030 nm, overlapping with the laser wavelengths employed in the photothermolysis investigation.

The EDX spectrum (Figure S2) confirmed the presence of silver through the Lα (2.98 keV) and Lβ (3.21 keV) peaks and of gold through the Lα (9.71 keV) and Mα (2.173 keV) peaks. An additional Lα peak at 0.93 keV originated from the copper grid of the TEM sample holder. These observations are consistent with the expected composition of AuAgNShs. Quantitative analysis of the EDX data indicated atomic fractions of 68% Au and 32% Ag. Zeta potential measurement, performed with a Nicomp Model 380 ZLS, was used to evaluate the surface charge of AuAgNShs in water. The average zeta potential was −35.9 ± 0.7 mV, consistent with a negative charge gold shell. The high zeta potential value agrees with a hypothesis in which the presence of surface charges stabilizes the NPs in aqueous solution, inhibiting aggregation and precipitation.[49−51]

Using XPS, we investigated the surface composition of AuAgNShs. Figure 2a presents the high-resolution XPS spectrum of the Au 4f binding energy region with the lower-energy peak at 84.0 eV used as the reference. Figure 2b demonstrates that the Ag 3d peak appears as a doublet with a binding energy of Ag $3d_{5/2}$ positioned at 368.2 eV and a 6 eV doublet splitting (at ∼374.2 eV). Figure 2c,d shows a minor peak at around 531 and 285 eV, respectively, which corresponds to the inevitable presence of organic contaminants, which always have a carbon−oxygen functional group.

Adsorption of Thiol Methacryloxypropyl T-Structure Siloxane (MAPTSiSH) Molecules onto AuAgNShs. To incorporate AuAgNShs for facilitating the photothermal modification of model catheter surfaces, siloxane-modified AuAgNShs were synthesized by chemisorption. Functionaliza-

https://doi.org/10.1021/acsami.5c11932
ACS Appl. Mater. Interfaces 2025, 17, 64065−64076

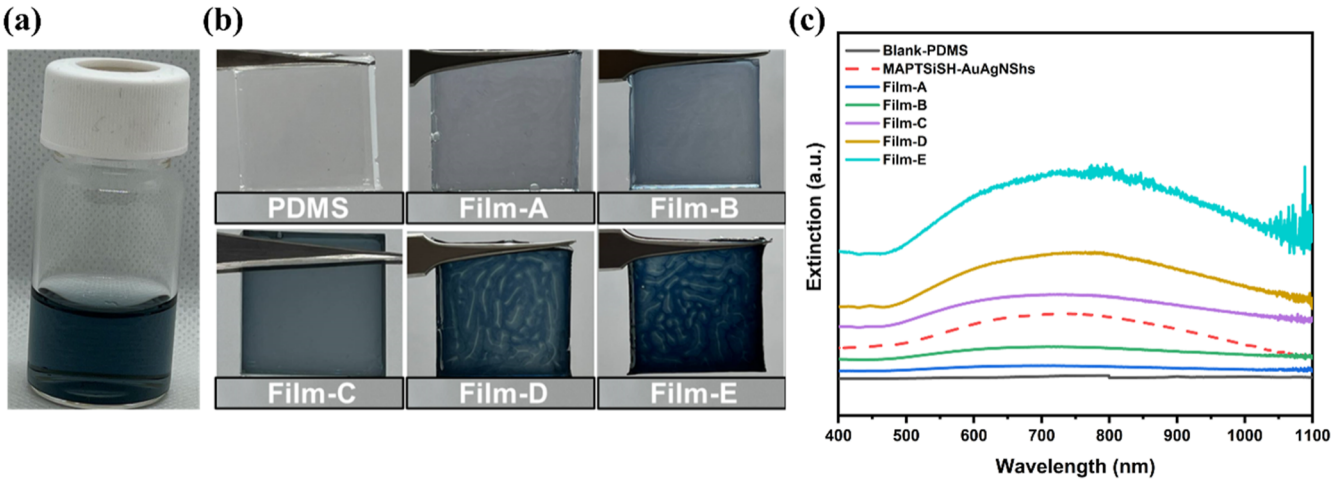

Figure 3. (a) Colloidal AuAgNSh suspension in EtOH, (b) blank PDMS and AuAgNSh-modified PDMS films labeled as Film-A to Film-E, where the loading content is gradually increased, and (c) extinction spectra of colloidal AuAgNShs (dashed line), PDMS (solid black line), and Film-A to Film-E.

tion of the AuAgNShs with the PDMS-like molecule (MAPTSiSH) yielded siloxane-modified AuAgNShs with good colloidal stability, enabling functionalized particles without aggregation in both aqueous and ethanoic media and a compatible environment for embedding in PDMS, generating a monodisperse distribution of particles in PDMS films. To highlight the necessity of functionalizing AuAgNShs for producing monodisperse AuAgNSh-PDMS films, we first combined nonfunctionalized AuAgNShs in a 10:1 ratio with the elastomer and cross-linker. Prior to the completion of oven curing, the AuAgNSh particles aggregated as illustrated in Figure S3, which shows the PDMS mixture containing nonfunctionalized nanoshells before curing compared to the analogous mixture containing MAPTSiSH-functionalized nanoshells.

XPS analysis was performed to verify the covalent binding of the siloxane organosulfur ligands to the AuAgNSh surfaces. Figure 2 shows the XPS spectra of MAPTSiSH-functionalized and nonfunctionalized AuAgNShs, with signals corresponding to Au, Ag, S, C, O, and Si. Because the sulfur binding energy (S 2p region) is indicative of the Au−S bond,[52] this region was examined in detail (Figure S4). Variations in the chemical and electrical states of sulfur give rise to distinct spectral features, allowing differentiation between covalently bound, unbound, and oxidized sulfur species.[52] The S 2p peak for bound thiols is a 2:1 doublet consisting of S $2p_{3/2}$ and S $2p_{1/2}$, with S $2p_{3/2}$ located at ∼162 eV. The binding energy of the S $2p_{3/2}$ peak of unbound thiols is ∼163 eV, while that of oxidized sulfur species is ∼167−169 eV.[52] The S 2p spectra of the MAPTSiSH-functionalized AuAgNShs are dominated by bound thiols, as indicated by the S $2p_{3/2}$ peak at 161.9 eV; there is no evidence of highly oxidized sulfur species in the samples. However, the S 2p portion of the spectrum displays some complexity. The amount of sulfur bound to the MAPTSiSH-functionalized AuAgNShs was quantified by deconvoluting the S 2p peaks following the procedure described in Figure S4. The analysis indicated that 68% of the thiol groups were bound, while 32% remained unbound. Furthermore, the presence of peaks for S 2p and Si 2p in the XPS data for MAPTSiSH-functionalized AuAgNShs and their absence in the XPS data for nonfunctionalized AuAgNShs provide further evidence of the adsorption of the thiol-terminated siloxanes on the MAPTSiSH-treated AuAgNShs.

The modification of AuAgNShs with an organosulfur siloxane coating causes a blueshift in the LSPR peak wavelength (see Figure 1d). This finding shows that the adsorption of thiol compounds alters the local dielectric environment and has an impact on the light absorption/scattering properties. In addition to our XPS and extinction investigation of functionalized and nonfunctionalized AuAgNShs, we observed an increase in the magnitude of the zeta potential of the MAPTSiSH-modified AuAgNShs, from −35.9 mV to −41.2 mV, which can be attributed to the strongly negative zeta potential value of PDMS.[53]

Solvent Stability Study. To determine the optimal solvent for dispersing AuAgNShs in the PDMS matrix and making uniformly dispersed films, we initially evaluated 10 solvents by combining 1 mL of each solvent with an elastomer and curing agent to produce blank PDMS matrices. After curing the mixture overnight in the oven, six of ten different solvents, including EtOH, MeOH, hexane, diethyl ether, $CHCl_3$, and o-xylene produced high-quality and transparent PDMS films free of bubbles and deformation (Figure S5a). Then, we examined the stability of MAPTSiSH-functionalized AuAgNShs in these six solvents to determine the ideal solvent for encapsulating the nanoshells within the PDMS matrix. EtOH was the only solvent in which the AuAgNShs remained stable for multiple hours, as illustrated in Figure S5b.

Preparation and Characterization of AuAgNSh-Modified PDMS Surfaces. To conduct photothermal studies on AuAgNSh-modified model catheter surfaces, NP solutions comprised of five selected volumes (0, 30, 60, 90, 120, and 150 μL) of a colloidal suspension of MAPTSiSH-AuAgNShs in 300 μL of EtOH were added to an elastomer/cross-linker mixture. The mixture was stirred until the particles were fully dispersed; then, it was transferred to a 3 cm × 3 cm blot box container and cured overnight at 50 °C. Quantities of elastomer and cross-linker were calculated to give prototypes having a 3 cm × 3 cm diameter and a 2 mm thickness. Following the curing procedure, homogeneous films with blue color were produced, the intensity of which increased with increasing amounts of MAPTSiSH-AuAgNShs (Figure 3a,b). Figure 3c shows the UV−vis−NIR spectra acquired for samples at various

https://doi.org/10.1021/acsami.5c11932
ACS Appl. Mater. Interfaces 2025, 17, 64065−64076

concentrations along with spectra of plain PDMS (black solid line) and a colloidal AuAgNSh suspension in EtOH (dashed line). Using a NanoSight NS300, the number of particles for 5 μL of MAPTSiSH-AuAgNShs in 2 mL of water was determined to be $1.73 \times 10^9 \pm 1.40 \times 10^8$, and beginning with 30 μL of functionalized NPs in Film-A, we can estimate the particle number density in each film, starting with $2.07 \times 10^{13} \pm 1.7 \times 10^{12}$ (Film-A), $4.15 \times 10^{13} \pm 3.4 \times 10^{12}$ (Film-B), $6.21 \times 10^{13} \pm 5.0 \times 10^{12}$ (Film-C), $8.31 \times 10^{13} \pm 6.7 \times 10^{12}$ (Film-D), and $10.35 \times 10^{13} \pm 8.4 \times 10^{12}$ (Film-E). Importantly, the extinction intensity of the PDMS samples increased with an increasing MAPTSiSH-AuAgNSh concentration. Coating the AuAgNShs with MAPTSiSH and embedding them in PDMS has the overall effect of broadening the LSPR wavelength to between 500 and 900 nm. However, the LSPR characteristics typical of AuAgNShs are preserved, indicating that the morphology of AuAgNShs did not change during the embedding and PDMS curing processes. Further supporting evidence is provided in Figure S6, which shows 10 UV−vis−NIR spectra taken at 10 distinct points of Film-D (concentration: $8.31 \times 10^{13} \pm 6.7 \times 10^{12}$ particles per mL), indicating that the dispersion of AuAgNShs in the polymer matrix of the film is homogeneous. Figure 3b provides photographs of each of the five films (Film-A to Film-E).

In addition, contact angles were measured for all samples, including a reference PDMS film prepared without embedded AuAgNShs. According to Table 1, there are no significant differences between the PDMS samples without MAPTSiSH-AuAgNShs and the PDMS samples containing increasing amounts of MAPTSiSH-AuAgNShs. Optical images of the advancing contact angles on the analyzed surfaces are shown in Figure S7. The data and corresponding images indicate that the surfaces of unmodified PDMS and AuAgNSh-modified PDMS are similar; therefore, bacterial attachment, growth, and eradication on both types of PDMS films are expected to be comparable.

Table 1. Advancing Contact Angles (θ_a, °) of PDMS and AuAgNSh-Modified PDMS Measured with Water

# of AuAgNShs per g elastomer	contact angle (deg)[a]
blank PDMS	103 ± 2
$2.07 \times 10^{13} \pm 1.7 \times 10^{12}$ **(Film-A)**	103 ± 2
$4.15 \times 10^{13} \pm 3.4 \times 10^{12}$ **(Film-B)**	103 ± 2
$6.21 \times 10^{13} \pm 5.0 \times 10^{12}$ **(Film-C)**	106 ± 2
$8.31\times 10^{13} \pm 6.7 \times 10^{12}$ **(Film-D)**	107 ± 2
$10.35 \times 10^{13} \pm 8.4 \times 10^{12}$ **(Film-E)**	104 ± 2

[a]Contact angle values represent the average of at least 9 measurements, reproducible within ±2°.

Photothermal Properties. After analyzing the spectra of PDMS samples containing increasing loading content of embedded MAPTSiSH-AuAgNShs, we investigated the samples' responses to NIR light. To evaluate the photothermal behavior of the samples, we utilized an 808 nm laser, which is often used for photothermal NIR irradiation.[32] Figure 4a displays thermograms obtained from five samples (Film-A to Film-E) with variable loading content of MAPTSiSH-AuAgNShs and a PDMS sample without NPs (blank). These thermograms suggest a direct and proportional relationship between the MAPTSiSH-AuAgNShs loading content and the hyperthermic effect. Notably, the temperature of the most concentrated sample increased by over 68 °C in less than 1 min, demonstrating a rapid and significant photothermal response. The temperatures reported were obtained by irradiating five distinct 1 cm film locations with 800 mW of power and averaging the results. All samples were also subjected to various laser intensities, and as depicted in Figure 4b, a linear correlation was observed between the applied power and the resulting temperature increase for all samples. Our photothermal heating outcomes are comparable to those of our previous study in which the temperature distribution and evolution of AuNShs populated on a PDMS surface was investigated.[32] In that study, AuNShs were used to modify the surface of PDMS, and the environment surrounding the AuNShs heated up rapidly as a result of the strong heat production by the AuNShs, which was caused by the absorption of laser energy via the LSPR. However, multiple steps were required to distribute the NPs on the surface of PDMS because the surface of PDMS required multiple activation steps before the AuNShs. By encapsulating functionalized NPs in a PDMS matrix, we were able to omit multiple steps and obtain extremely stable films (vide infra).

Figure 4b shows that the temperature increase (ΔT) scales linearly with laser power; thus, the heating rate can be reduced proportionally. Extrapolation of this linear trend indicates that an ANSI-compliant irradiance of 0.2 W cm^{-2} would still bring the surface to the ≥50 °C bactericidal threshold, requiring a few minutes rather than ∼60 s of irradiation. Consequently, the photothermal mechanism remains compatible with current safety regulations governing skin exposure. Our use of 800 mW cm^{-2} was solely to shorten the proof-of-concept experiment; the data demonstrate that comparable antimicrobial efficacy is attainable within regulatory limits.

To assess the photothermal stability of the modified films, we exposed the film with the highest loading content of NPs (Film-E) to 800 mW of NIR radiation for 50 min while monitoring the temperature (Figure 4c). We found only a slight decrease in temperature during the entire irradiation process, confirming the stability of the film. This observation also suggests that the irradiation did not alter the morphology of the NPs significantly, which in turn did not affect the light-to-heat conversion process, which would have lessened the photothermal effect. We further evaluated the film stability by subjecting Film-E to a heating−cooling process over 15 cycles, each consisting of 2 min of irradiation at 800 mW cm^{-2} followed by 2 min of rest (Figure 4d). During these cycles, we observed no significant changes in the maximum temperature. These results demonstrate the exceptional photothermal stability of the film and its rapid cooling−heating process (i.e., the surface temperature increased to over 68 °C within 1 min of NIR illumination, which was rapidly reversible). Additionally, no temperature change was observed in the blank PDMS sample, indicating that the laser alone did not heat the polymer films (e.g., compare Figure 4e with Figure 4f and Video S1 with Video S2).

Bacterial Adherence Assay with Pathogenic *E. faecalis*. After the successful generation of AuAgNSh-modified PDMS with defined photothermal properties, these model catheter materials were evaluated as platforms for photothermal eradication of pathogenic bacteria. To determine the exposure time required to achieve bactericidal heating, a photothermal killing experiment was conducted using an 800 mW, 810 nm NIR diode laser. Seven sets of samples were prepared by incubating *E. faecalis* at 37 °C for 72 h with small strips (0.2 cm × 1 cm) of AuAgNSh-modified PDMS, along

https://doi.org/10.1021/acsami.5c11932
ACS Appl. Mater. Interfaces 2025, 17, 64065−64076

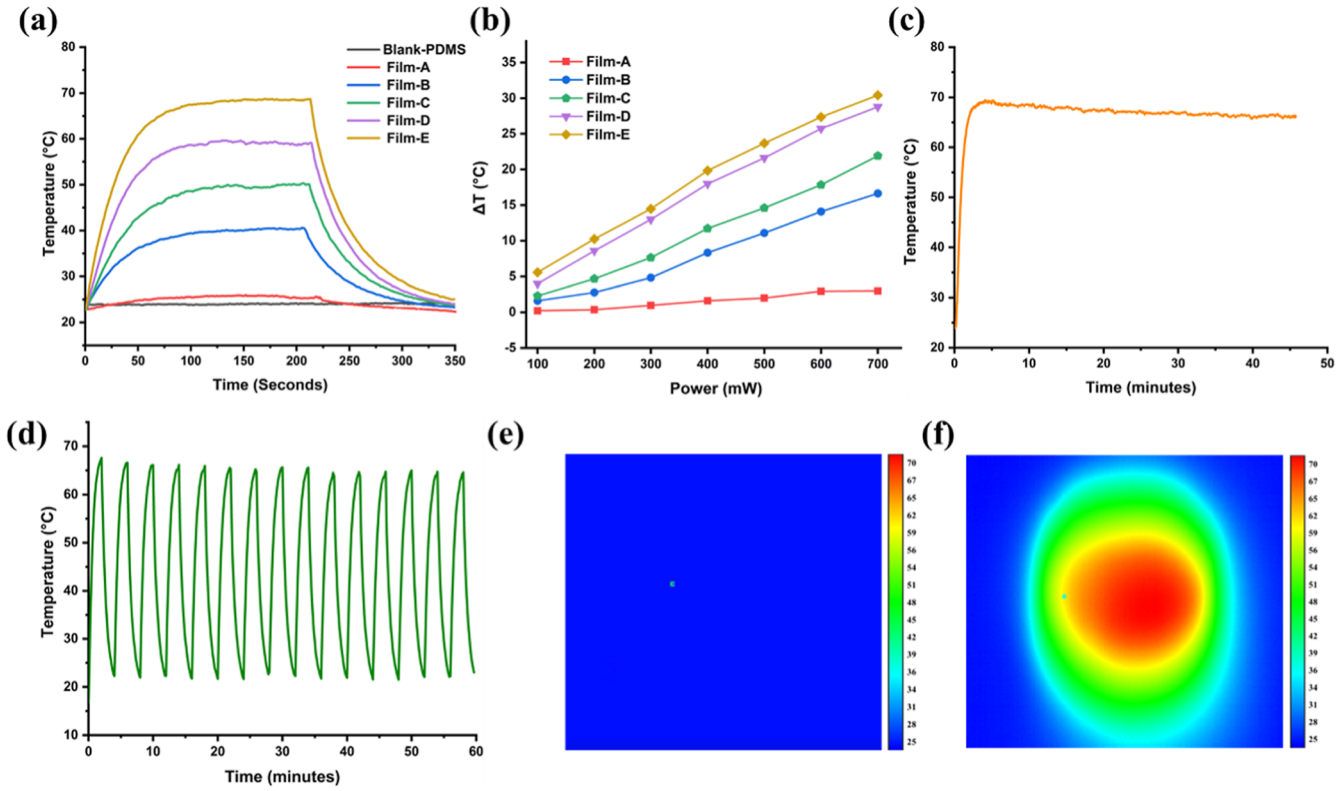

Figure 4. (a) Photothermal heating curves for PDMS and Films A–E, (b) change in temperature (ΔT) as a function of applied power for PDMS samples containing embedded MAPTSiSH-AuAgNShs at increasing loading contents (Film-A, red; Film-B, blue; Film-C, green; Film-D, purple; and Film-E, yellow), showing linear dependence, (c) time-dependent temperature profile of Film-E over 50 min at 800 mW laser power, (d) time-dependent temperature profile of Film-E under 800 mW, 810 nm laser irradiation over 15 on/off cycles, and (e) thermal image of Film-E before and (f) after NIR exposure.

with a control PDMS surface lacking MAPTSiSH-AuAgNShs. Bright-field optical microscopy (Figure S8) revealed that *E. faecalis* surface coverage exceeded 50% on both modified and unmodified surfaces.

Two sets of samples were exposed to laser irradiation for varying durations (10, 20, 40, 60, 240, 420, and 600 s), while the seventh set remained unexposed. Following our previously described method,[32] bacterial survival on the surfaces was assessed by colony formation assay. Bacteria were detached by sonication in 0.01% SDS solution, followed by vortexing for 2 min at 2000 rpm. The resulting suspension was serially diluted and plated in duplicate on LB agar. After 24 h of incubation at 37 °C, colony counts were recorded. Figure 5 shows representative images from the colony formation assays on AuAgNSh-modified PDMS surfaces before and after NIR irradiation along with bar graphs presenting the average colony counts from seven independent experiments performed in duplicate. Given that each strip that we quantified has an active surface area of only 0.20 cm^2 (0.2 cm × 1 cm), the values plotted therefore correspond to ≈10^6 CFU cm^{-2}. In comparison to the control sample, the number of surviving *E. faecalis* on AuAgNSh-modified PDMS surfaces decreased significantly after 60 s of NIR illumination. After 420 and 600 s of laser irradiation, the results were even more obvious; all bacteria had been killed by laser irradiation in 420 s within statistical error. These results indicate that the hyperthermia strategy is effective against pathogen colonization and may represent an alternative method to combat antibiotic-resistant bacteria. The reduction in bacterial colonies is attributed to plasmonic thermally induced damage. The overall heat generated by the plasmonic photothermal method is sufficient to destroy the bacteria attached to the surfaces of the model catheters.

To confirm the efficacy of the photothermal heating protocol in lysing bacteria on AuAgNSh-modified PDMS films, SEM was used to examine bacterial morphology before and after 420 s of NIR irradiation. As shown in Figure 6, films exposed to NIR light exhibited evidence of localized hyperthermia induced by the LSPR response of AuAgNShs, resulting in thermal decomposition and rupture of the *E. faecalis* cell wall. These findings indicate that an irradiation time of approximately 400 s is sufficient to induce heat-mediated damage in bacteria attached to nanoshell-modified PDMS films.

The effectiveness of thermal treatment is determined by two factors: the degree of temperature increase above the biological norm and the duration of the treatment. Studies have shown that inducing an incremental temperature increase that causes irreversible tissue injury can be accomplished by raising the temperature of cells above 50 °C, which activates the coagulative necrosis process and leads to cell death.[54] When exposed to temperatures above 60 °C, proteins undergo denaturation, a process that causes them to permanently lose their structure and function.[55] Denaturation can occur very rapidly and is irreversible for most proteins. In addition, if tissues are exposed to temperatures above 80 °C, the water within them can evaporate, which leads to cell damage or rupture.[55]

In this study, we demonstrated that AuAgNSh-modified PDMS surfaces generated substantial temperature increases

https://doi.org/10.1021/acsami.5c11932
ACS Appl. Mater. Interfaces 2025, 17, 64065–64076

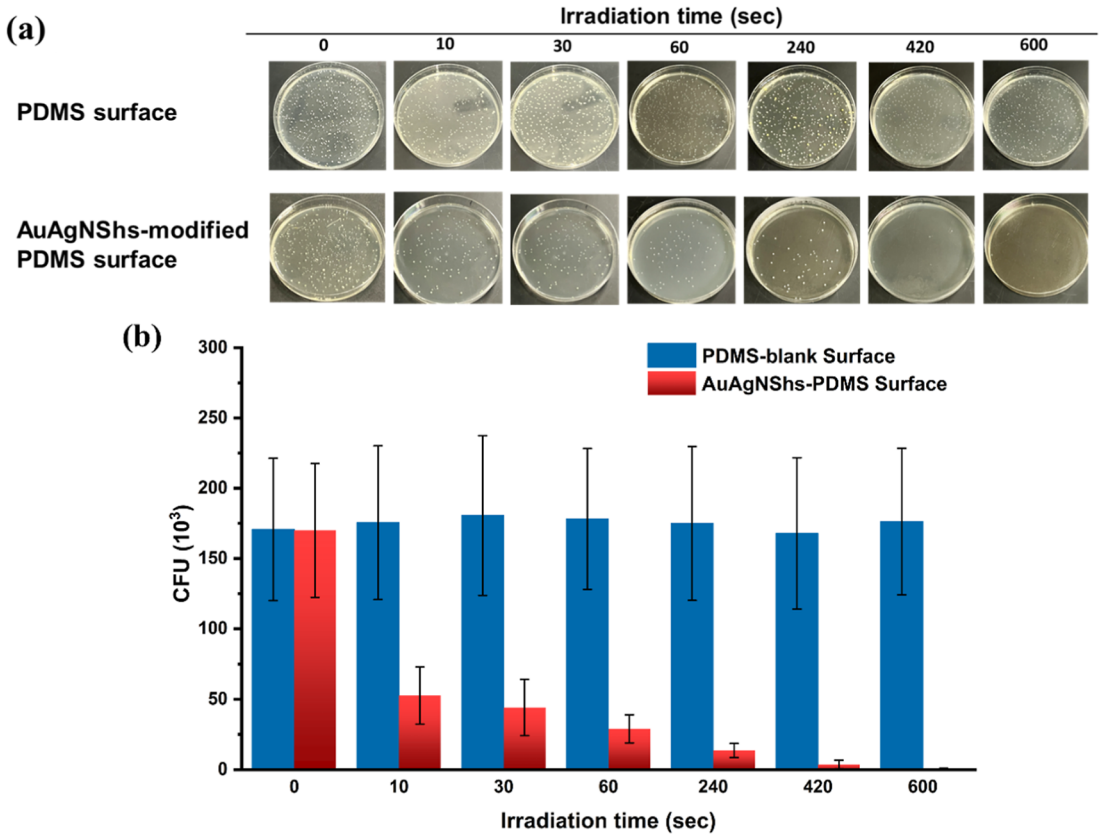

Figure 5. Colony formation assays of *E. faecalis* following NIR irradiation: (a) images of bacterial colonies on blank PDMS and AuAgNSh-modified PDMS surfaces at increasing exposure times, and (b) bar graphs showing average colony forming units (CFUs) from four independent experiments. Error bars represent ±SD (n = 4).

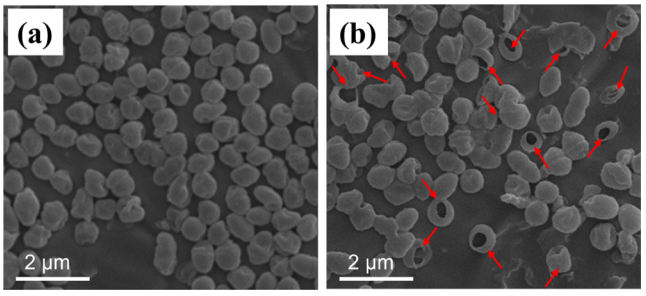

Figure 6. SEM images showing *E. faecalis* on AuAgNSh-modified PDMS surfaces (a) prior to and (b) after NIR irradiation.

under NIR irradiation. By variation of the loading content of AuAgNShs, different temperature levels were achieved, with a maximum localized surface temperature of 68 °C for the most concentrated film (Film-E), leading to bacterial cell death. AuNShs can absorb light and convert it into thermal energy efficiently, which can cause damage to bacterial cells. This thermal energy is rapidly transferred to the surrounding environment, including bacterial cells via plasmon-phonon relaxation.[56] When the temperature of bacterial cells rises, proteins and other biomolecules can become denatured, leading to cell damage and mortality. Additionally, the high temperature can alter the physical properties of the cell membrane, leading to membrane rupture and loss of integrity.[57] Hence, photothermal cell damage can be attributed to both thermal and mechanical factors. The effectiveness of this method depends on the dosage, type, and irradiation time of the laser used, as well as the subcellular location of the NPs.[58]

Researchers have studied the mechanisms of cell death induced by photothermal therapy through NPs to some extent. For example, Zharov and colleagues explored how laser pulses can damage cells by causing a series of phenomena, such as protein denaturation or breakdown, cell cavitation, cellular structure rupture, evaporation of cellular liquid, and bubble formation due to shock waves caused by particle thermal expansion, evaporation, optical breakdown, or plasma generation of AuNPs.[59] While previous studies have demonstrated the effectiveness of AuNP-mediated photothermal disruption of cellular structures,[32,38,60,61] our results show that AuAgNShs can similarly induce photothermal cell rupture, effectively eliminating bacteria in model catheter materials.

CONCLUSIONS

This study demonstrated an effective photothermal platform for eradicating pathogenic *E. faecalis* within ∼400 s in an in vitro assay using PDMS model catheter films. This system is stable and reusable for multiple cycles. When combined with NIR irradiation, the AuAgNSh-modified surfaces offer a potential broad-spectrum antibiotic that kills adhered pathogens rapidly. This method relies on the heat produced by AuAgNShs in response to NIR irradiation and the transfer of thermal energy to the bacteria. This hyperthermia strategy has potential as a therapeutic approach in applications where NIR light can access the catheter, either through tissue or directly via a fiber-optic cable. In the present system, the NIR source operates at 810 nm, which penetrates human tissue to a

https://doi.org/10.1021/acsami.5c11932
ACS Appl. Mater. Interfaces 2025, 17, 64065−64076

depth of 2−4 mm depending on laser intensity.[62,63] To further improve efficacy, additional studies are needed to optimize the absorption maxima of AuAgNShs in relation to the applied NIR wavelength and power, with the ultimate goal of enabling in vivo catheter treatment using NIR light.

■ ASSOCIATED CONTENT

Supporting Information

The Supporting Information is available free of charge at https://pubs.acs.org/doi/10.1021/acsami.5c11932.

SEM image of Ag nanospheres, EDX spectrum of AuAgNShs, optical images of mixtures containing PDMS with AuAgNShs and MAPTSiSH-AuAgNShs, deconvolution of the XPS S 2p region for MAPTSiSH-AuAgNShs, optical images of the solvent study, UV−vis−NIR spectra of a PDMS-AuAgNSh composite, optical images of the advancing contact angles of blank PDMS and AuAgNSh-modified PDMS films, and reflected bright-field images of *E. faecalis* obtained after an incubation for 72 h with PDMS and AuAgNSh-modified PDMS (PDF)

Time-lapse videos of NIR irradiation of unmodified PDMS (MPG)

Nanoshell-modified PDMS (MPG)

■ AUTHOR INFORMATION

Corresponding Authors

Naihao Chiang − *Department of Chemistry, University of Houston, Houston, Texas 77204-5003, United States;* orcid.org/0000-0003-3782-6546; Email: nchiang@central.uh.edu

T. Randall Lee − *Department of Chemistry, University of Houston, Houston, Texas 77204-5003, United States; The Texas Center for Superconductivity, University of Houston, Houston, Texas 77204-5003, United States;* orcid.org/0000-0001-9584-8861; Email: trlee@uh.edu

Authors

Mina Omidiyan − *Department of Chemistry, University of Houston, Houston, Texas 77204-5003, United States; The Texas Center for Superconductivity, University of Houston, Houston, Texas 77204-5003, United States;* orcid.org/0000-0002-5017-5269

Mengfan Wang − *Department of Chemistry, University of Houston, Houston, Texas 77204-5003, United States*

Pooria Tajalli − *Department of Chemistry, University of Houston, Houston, Texas 77204-5003, United States; The Texas Center for Superconductivity, University of Houston, Houston, Texas 77204-5003, United States;* orcid.org/0000-0001-7415-0587

Xing He − *Department of Chemistry, University of Houston, Houston, Texas 77204-5003, United States;* orcid.org/0000-0001-5341-5662

Supawitch Hoijang − *Department of Chemistry, University of Houston, Houston, Texas 77204-5003, United States; The Texas Center for Superconductivity, University of Houston, Houston, Texas 77204-5003, United States;* orcid.org/0000-0002-0061-5166

Chengzhi Cai − *Department of Chemistry, University of Houston, Houston, Texas 77204-5003, United States;* orcid.org/0000-0001-9800-7769

Complete contact information is available at: https://pubs.acs.org/10.1021/acsami.5c11932

Notes

The authors declare no competing financial interest.

■ ACKNOWLEDGMENTS

T.R.L. thanks the Robert A. Welch Foundation (grant nos. V-E-0001 and E-1320) for generous financial support and the National Science Foundation (CHE-2109174) for supporting the design and synthesis of the MAPTSiSH compatibilizing agent. N.C. is grateful for support from the National Institute of Biomedical Imaging and Bioengineering (grant R00EB028325). C.C. thanks the National Science Foundation (DMR-2005199) for support.

■ REFERENCES

(1) Ananda, T.; Modi, A.; Chakraborty, I.; Managuli, V.; Mukhopadhyay, C.; Mazumder, N. Nosocomial Infections and Role of Nanotechnology. *Bioengineering* **2022**, *9*, 51.

(2) Pérez-Granda, M. J.; Carrillo, C. S.; Rabadán, P. M.; Valerio, M.; Olmedo, M.; Muñoz, P.; Bouza, E. Increase in the Frequency of Catheter-Related Bloodstream Infections during the COVID-19 Pandemic: A Plea for Control. *J. Hosp. Infect.* **2022**, *119*, 149−154.

(3) Nimer, N. A. Nosocomial Infection and Antibiotic-Resistant Threat in the Middle East. *Infect. Drug Resist.* **2022**, *15*, 631−639.

(4) Zhong, Y.; Zhou, L.; Liu, X.; Deng, L.; Wu, R.; Xia, Z.; Mo, G.; Zhang, L.; Liu, Z.; Tang, J. Incidence, Risk Factors, and Attributable Mortality of Catheter-Related Bloodstream Infections in the Intensive Care Unit After Suspected Catheters Infection: A Retrospective 10-Year Cohort Study. *Infect. Dis. Ther.* **2021**, *10*, 985−999.

(5) Chadha, J.; Thakur, N.; Chhibber, S.; Harjai, K. A Comprehensive Status Update on Modification of Foley Catheter to Combat Catheter-Associated Urinary Tract Infections and Microbial Biofilms. *Crit. Rev. Microbiol.* **2024**, *50*, 168−195.

(6) van den Bosch, C. H.; van Woensel, J.; van de Wetering, M. D. Prophylactic Antibiotics for Preventing Gram-Positive Infections Associated with Long-Term Central Venous Catheters in Adults and Children Receiving Treatment for Cancer. *Cochrane Database Syst. Rev.* **2021**, *10*, CD003295.

(7) Sheng, K. X.; Zhang, P.; Li, J. W.; Cheng, J.; He, Y. C.; Böhlke, M.; Chen, J. H. Comparative Efficacy and Safety of Lock Solutions for the Prevention of Catheter-Related Complications Including Infectious and Bleeding Events in Adult Haemodialysis Patients: A Systematic Review and Network Meta-Analysis. *Clin. Microbiol. Infect.* **2020**, *26*, 545−552.

(8) Tejada, S.; Leal-dos-Santos, M.; Peña-López, Y.; Blot, S.; Alp, E.; Rello, J. Antiseptic Barrier Caps in Central Line-Associated Bloodstream Infections: A Systematic Review and Meta-Analysis. *Eur. J. Intern. Med.* **2022**, *99*, 70−81.

(9) Munoz-Mozas, G. Preventing Intravenous Catheter-Related Bloodstream Infections (CRBSIs). *Br. J. Nurs.* **2023**, *32*, S4−S10.

(10) Chakrabarty, S.; Mishra, M. P.; Bhattacharyay, D. Targeting Microbial Bio-Film: An Update on MDR Gram-Negative Bio-Film Producers Causing Catheter-Associated Urinary Tract Infections. *Appl. Biochem. Biotechnol.* **2022**, *194*, 2796−2830.

(11) Gebreyohannes, G.; Nyerere, A.; Bii, C.; Sbhatu, D. B. Challenges of Intervention, Treatment, and Antibiotic Resistance of Biofilm-Forming Microorganisms. *Heliyon* **2019**, *5*, No. e02192.

(12) Sharma, D.; Misba, L.; Khan, A. U. Antibiotics versus Biofilm: An Emerging Battleground in Microbial Communities. *Antimicrob. Resist. Infect. Control* **2019**, *8*, 76.

(13) Karnwal, A.; Kumar, G.; Pant, G.; Hossain, K.; Ahmad, A.; Alshammari, M. B. Perspectives on Usage of Functional Nanomaterials in Antimicrobial Therapy for Antibiotic-Resistant Bacterial Infections. *ACS Omega* **2023**, *8*, 13492−13508.

(14) Kobayashi, R. K. T.; Nishio, E. K.; Scandorieiro, S.; Saikawa, G. I. A.; da Rocha, S. P. D.; Nakazato, G. Metallic Nanoparticles as a

Potential Antimicrobial for Catheters and Prostheses. In *Materials for Biomedical Engineering*; Holban, A.-M., Grumezescu, A. M., Eds.; Elsevier, 2019; pp 153−196.
(15) Teixeira-Santos, R.; Gomes, L. C.; Mergulhão, F. J. M. Recent Advances in Antimicrobial Surfaces for Urinary Catheters. *Curr. Opin. Biomed. Eng.* **2022**, *22*, 100394.
(16) Goda, R. M.; El-Baz, A. M.; Khalaf, E. M.; Alharbi, N. K.; Elkhooly, T. A.; Shohayeb, M. M. Combating Bacterial Biofilm Formation in Urinary Catheter by Green Silver Nanoparticle. *Antibiotics* **2022**, *11*, 495.
(17) Divya, M.; Kiran, G. S.; Hassan, S.; Selvin, J. Biogenic Synthesis and Effect of Silver Nanoparticles (AgNPs) to Combat Catheter-Related Urinary Tract Infections. *Biocatal. Agric. Biotechnol.* **2019**, *18*, 101037.
(18) Burduşel, A.-C.; Gherasim, O.; Grumezescu, A. M.; Mogoantă, L.; Ficai, A.; Andronescu, E. Biomedical Applications of Silver Nanoparticles: An Up-to-Date Overview. *Nanomaterials* **2018**, *8*, 681.
(19) Karchmer, T. B.; Giannetta, E. T.; Muto, C. A.; Strain, B. A.; Farr, B. M. A Randomized Crossover Study of Silver-Coated Urinary Catheters in Hospitalized Patients. *Arch. Intern. Med.* **2000**, *160*, 3294−3298.
(20) Priyadarshi, N.; Kaushal, S.; Garg, P.; Sagar, P.; Gupta, R.; Kaur, J.; Kumar, A.; Kumar, S.; Singhal, N. K. Advances in Photothermal Therapy for Cancer and Bacterial Cells Ablation Using Various Nanomaterials. *Adv. Colloid Interface Sci.* **2025**, *342*, 103541.
(21) Bai, X.; Yang, Y.; Zheng, W.; Huang, Y.; Xu, F.; Bao, Z. Synergistic Photothermal Antibacterial Therapy Enabled by Multifunctional Nanomaterials: Progress and Perspectives. *Mater. Chem. Front.* **2023**, *7*, 355−380.
(22) Park, E.; Selvaraj, R.; Kim, Y. High-Efficiency Photothermal Sterilization on PDMS Film with Au@CuS Yolk-Shell Nanoparticles. *J. Ind. Eng. Chem.* **2022**, *113*, 522−529.
(23) Ouyang, B.; Wei, D.; Wu, B.; Yan, L.; Gang, H.; Cao, Y.; Chen, P.; Zhang, T.; Wang, H. In the View of Electrons Transfer and Energy Conversion: The Antimicrobial Activity and Cytotoxicity of Metal-Based Nanomaterials and Their Applications. *Small* **2024**, *20*, 2303153.
(24) Zhang, D.; Kukkar, D.; Bhatt, P.; Kim, K.-H.; Kaur, K.; Wang, J. Novel Nanomaterials-Based Combating Strategies against Drug-Resistant Bacteria. *Colloids Surf., B* **2025**, *248*, 114478.
(25) Doveri, L.; Diaz Fernandez, Y. A.; Dacarro, G. Nanomaterials for Photothermal Antimicrobial Surfaces. *ACS Omega* **2024**, *9*, 25575−25590.
(26) Omidiyan, M.; Srinoi, P.; Tajalli, P.; Lee, T. R. Review of Light-Activated Antimicrobial Nanoparticle−Polymer Composites for Biomedical Devices. *ACS Appl. Nano Mater.* **2024**, *7*, 8377−8391.
(27) Chen, Y.; Zhou, F.; Wang, C.; Hu, L.; Guo, P. Nanostructures as Photothermal Agents in Tumor Treatment. *Molecules* **2023**, *28*, 277.
(28) Dheyab, M. A.; Aziz, A. A.; Khaniabadi, P. M.; Jameel, M. S.; Oladzadabbasabadi, N.; Rahman, A. A.; Braim, F. S.; Mehrdel, B. Gold Nanoparticles-Based Photothermal Therapy for Breast Cancer. *Photodiagnosis Photodyn. Ther.* **2023**, *42*, 103312.
(29) Lv, Z.; He, S.; Wang, Y.; Zhu, X. Noble Metal Nanomaterials for NIR-Triggered Photothermal Therapy in Cancer. *Adv. Healthc. Mater.* **2021**, *10*, 2001806.
(30) Yang, W.; Xia, B.; Wang, L.; Ma, S.; Liang, H.; Wang, D.; Huang, J. Shape Effects of Gold Nanoparticles in Photothermal Cancer Therapy. *Mater. Today Sustain.* **2021**, *13*, 100078.
(31) Cheng, X.; Sun, R.; Yin, L.; Chai, Z.; Shi, H.; Gao, M. Light-Triggered Assembly of Gold Nanoparticles for Photothermal Therapy and Photoacoustic Imaging of Tumors In Vivo. *Adv. Mater.* **2017**, *29*, 1604894.
(32) Khantamat, O.; Li, C.-H.; Yu, F.; Jamison, A. C.; Shih, W.-C.; Cai, C.; Lee, T. R. Gold Nanoshell-Decorated Silicone Surfaces for the Near-Infrared (NIR) Photothermal Destruction of the Pathogenic Bacterium E. Faecalis. *ACS Appl. Mater. Interfaces* **2015**, *7*, 3981−3993.
(33) Ye, X.; Shi, H.; He, X.; Wang, K.; Li, D.; Qiu, P. Gold Nanorod-Seeded Synthesis of Au@Ag/Au Nanospheres with Broad and Intense Near-Infrared Absorption for Photothermal Cancer Therapy. *J. Mater. Chem. B* **2014**, *2*, 3667−3673.
(34) Liu, T.; Tian, J.; Chen, Z.; Liang, Y.; Liu, J.; Liu, S.; Li, H.; Zhan, J.; Yang, X. Anti-TROP2 Conjugated Hollow Gold Nanospheres as a Novel Nanostructure for Targeted Photothermal Destruction of Cervical Cancer Cells. *Nanotechnology* **2014**, *25*, 345103.
(35) Yu, M.; Guo, F.; Wang, J.; Tan, F.; Li, N. Photosensitizer-Loaded pH-Responsive Hollow Gold Nanospheres for Single Light-Induced Photothermal/Photodynamic Therapy. *ACS Appl. Mater. Interfaces* **2015**, *7*, 17592−17597.
(36) Huang, X.; El-Sayed, I. H.; Qian, W.; El-Sayed, M. A. Cancer Cell Imaging and Photothermal Therapy in the Near-Infrared Region by Using Gold Nanorods. *J. Am. Chem. Soc.* **2006**, *128*, 2115−2120.
(37) Jiang, T.; Song, J.; Zhang, W.; Wang, H.; Li, X.; Xia, R.; Zhu, L.; Xu, X. Au−Ag@Au Hollow Nanostructure with Enhanced Chemical Stability and Improved Photothermal Transduction Efficiency for Cancer Treatment. *ACS Appl. Mater. Interfaces* **2015**, *7*, 21985−21994.
(38) Hwang, S.; Nam, J.; Jung, S.; Song, J.; Doh, H.; Kim, S. Gold Nanoparticle-Mediated Photothermal Therapy: Current Status and Future Perspective. *Nanomed.* **2014**, *9*, 2003−2022.
(39) Odion, R.; Liu, Y.; Vo-Dinh, T. Plasmonic Gold Nanostar-Mediated Photothermal Immunotherapy. *IEEE J. Sel. Top. Quantum Electron.* **2021**, *27*, 1−9.
(40) Song, C.; Li, F.; Guo, X.; Chen, W.; Dong, C.; Zhang, J.; Zhang, J.; Wang, L. Gold Nanostars for Cancer Cell-Targeted SERS-Imaging and NIR Light-Triggered Plasmonic Photothermal Therapy (PPTT) in the First and Second Biological Windows. *J. Mater. Chem. B* **2019**, *7*, 2001−2008.
(41) Toci, G.; Olgiati, F.; Pallavicini, P.; Diaz Fernandez, Y. A.; De Vita, L.; Dacarro, G.; Grisoli, P.; Taglietti, A. Gold Nanostars Embedded in PDMS Films: A Photothermal Material for Antibacterial Applications. *Nanomaterials* **2021**, *11*, 3252.
(42) He, J.; Wei, Q.; Wang, S.; Hua, S.; Zhou, M. Bioinspired Protein Corona Strategy Enhanced Biocompatibility of Ag-Hybrid Hollow Au Nanoshells for Surface-Enhanced Raman Scattering Imaging and on-Demand Activation Tumor-Phototherapy. *Biomaterials* **2021**, *271*, 120734.
(43) Vongsavat, V.; Vittur, B. M.; Bryan, W. W.; Kim, J.-H.; Lee, T. R. Ultrasmall Hollow Gold−Silver Nanoshells with Extinctions Strongly Red-Shifted to the Near-Infrared. *ACS Appl. Mater. Interfaces* **2011**, *3*, 3616−3624.
(44) Mourdikoudis, S.; Pallares, R. M.; Thanh, N. T. K. Characterization Techniques for Nanoparticles: Comparison and Complementarity upon Studying Nanoparticle Properties. *Nanoscale* **2018**, *10*, 12871−12934.
(45) Omidiyan, M.; Tajalli, P.; Tran, H.-V.; Hoijang, S.; Lee, T. R. Siloxane-Terminated Self-Assembled Monolayers for Mimicking Nanoscale Hydrophobic Polydimethylsiloxane Surfaces. https://doi.org/10.1021/acs.langmuir.5c02908.
(46) Emori, T. G.; Gaynes, R. P. An Overview of Nosocomial Infections, Including the Role of the Microbiology Laboratory. *Clin. Microbiol. Rev.* **1993**, *6*, 428−442.
(47) Lee, P. C.; Meisel, D. Adsorption and Surface-Enhanced Raman of Dyes on Silver and Gold Sols. *J. Phys. Chem.* **1982**, *86*, 3391−3395.
(48) Srinoi, P.; Marquez, M. D.; Lee, T.-C.; Lee, T. R. Hollow Gold-Silver Nanoshells Coated with Ultrathin SiO_2 Shells for Plasmon-Enhanced Photocatalytic Applications. *Materials* **2020**, *13*, 4967.
(49) Liang, Z.; Liu, Y.; Ng, S. S.; Li, X.; Lai, L.; Luo, S.; Liu, S. The Effect of pH Value on the Formation of Gold Nanoshells. *J. Nanoparticle Res.* **2011**, *13*, 3301−3311.
(50) Cano, E.; Torres, C. L.; Bastidas, J. M. An XPS Study of Copper Corrosion Originated by Formic Acid Vapour at 40% and 80% Relative Humidity. *Mater. Corros.* **2001**, *52*, 667−676.

(51) Brinson, B. E.; Lassiter, J. B.; Levin, C. S.; Bardhan, R.; Mirin, N.; Halas, N. J. Nanoshells Made Easy: Improving Au Layer Growth on Nanoparticle Surfaces. *Langmuir* **2008**, *24*, 14166−14171.
(52) Castner, D. G.; Hinds, K.; Grainger, D. W. X-Ray Photoelectron Spectroscopy Sulfur 2p Study of Organic Thiol and Disulfide Binding Interactions with Gold Surfaces. *Langmuir* **1996**, *12*, 5083−5086.
(53) Song, Y.; Zhao, K.; Li, M.; Pan, X.; Li, D. A Novel Method for Measuring Zeta Potentials of Solid−Liquid Interfaces. *Anal. Chim. Acta* **2015**, *853*, 689−695.
(54) Zhang, Y.; Zhan, X.; Xiong, J.; Peng, S.; Huang, W.; Joshi, R.; Cai, Y.; Liu, Y.; Li, R.; Yuan, K.; Zhou, N.; Min, W. Temperature-Dependent Cell Death Patterns Induced by Functionalized Gold Nanoparticle Photothermal Therapy in Melanoma Cells. *Sci. Rep.* **2018**, *8*, 8720.
(55) Yun, W. S.; Park, J.-H.; Lim, D.-K.; Ahn, C.-H.; Sun, I.-C.; Kim, K. How Did Conventional Nanoparticle-Mediated Photothermal Therapy Become "Hot" in Combination with Cancer Immunotherapy? *Cancers* **2022**, *14*, 2044.
(56) Jaque, D.; Martínez Maestro, L.; del Rosal, B.; Haro-Gonzalez, P.; Benayas, A.; Plaza, J. L.; Martín Rodríguez, E.; García Solé, J. Nanoparticles for Photothermal Therapies. *Nanoscale* **2014**, *6*, 9494−9530.
(57) Yougbaré, S.; Mutalik, C.; Krisnawati, D. I.; Kristanto, H.; Jazidie, A.; Nuh, M.; Cheng, T.-M.; Kuo, T.-R. Nanomaterials for the Photothermal Killing of Bacteria. *Nanomaterials* **2020**, *10*, 1123.
(58) Huang, X.; El-Sayed, M. A. Plasmonic Photo-Thermal Therapy (PPTT). *Alex. J. Med.* **2011**, *47*, 1−9.
(59) Pustovalov, V. K.; Smetannikov, A. S.; Zharov, V. P. Photothermal and Accompanied Phenomena of Selective Nanophotothermolysis with Gold Nanoparticles and Laser Pulses. *Laser Phys. Lett.* **2008**, *5*, 775.
(60) Taylor, M. L.; Wilson, R. E.; Amrhein, K. D.; Huang, X. Gold Nanorod-Assisted Photothermal Therapy and Improvement Strategies. *Bioengineering* **2022**, *9*, 200.
(61) Camacho, S. A.; Kobal, M. B.; Moreira, L. G.; Bistaffa, M. J.; Roque, T. C.; Pazin, W. M.; Toledo, K. A.; Oliveira, O. N.; Aoki, P. H. B. The Efficiency of Photothermal Action of Gold Shell-Isolated Nanoparticles against Tumor Cells Depends on Membrane Interactions. *Colloids Surf. B Biointerfaces* **2022**, *211*, 112301.
(62) Henderson, T. A.; Morries, L. D. Near-Infrared Photonic Energy Penetration: Can Infrared Phototherapy Effectively Reach the Human Brain? *Neuropsychiatr. Dis. Treat.* **2015**, *11*, 2191−2208.
(63) Henderson, T. A. Can Infrared Light Really Be Doing What We Claim It Is Doing? Infrared Light Penetration Principles, Practices, and Limitations. *Front. Neurol.* **2024**, *15*, 1398894.

https://doi.org/10.1021/acsami.5c11932
ACS Appl. Mater. Interfaces 2025, 17, 64065−64076